R. Kovacevic
Mem. ASME

Y. M. Zhang
Mem. ASME

Welding Research and
Development Laboratory,
Center for Robotics and
Manufacturing Systems and,
Department of Mechanical Engineering,
University of Kentucky,
Lexington, KY

Real-Time Image Processing for Monitoring of Free Weld Pool Surface

The arc weld pool is always deformed by plasma jet. In a previous study, a novel sensing mechanism was proposed to sense the free weld pool surface. The specular reflection of pulsed laser stripes from the mirror-like pool surface was captured by a CCD camera. The distorted laser stripes clearly depicted the 3D shape of the free pool surface. To monitor and control the welding process, the on-line acquisition of the reflection pattern is required. In this work, the captured image is analyzed to identify the torch and electrode. The weld pool edges are then detected. Because of the interference of the torch and electrode, the acquired pool boundary may be incomplete. To acquire the complete pool boundary, models have been fitted using the edge points. Finally, the stripes reflected from the weld pool are detected. Currently, the reflection pattern and pool boundary are being related to the weld penetration and used to control the weld penetration.

1 Introduction

Strictly speaking, no flat weld pool surfaces exist in arc welding processes. Pool surface deformation can always be observed in gas metal arc welding (GMAW) and gas tungsten arc welding (GTAW) with filler, due to the mass transfer. For GTAW without filler, pool surface deformation is apparent in the full penetration mode. In the case of partial penetration, three modes of pool deformation can be observed for different current levels [1]. Thus, the deformation of the pool surface is an inherent characteristic of arc welding processes. The observation of the weld pool surface is, therefore, essential and necessary for studying welding processes. Furthermore, surface deformation is an important phenomenon in the arc welding process because of its influence on the arc energy distribution [1, 2], its correlation with possible weld defects [2], and correlation to the weld penetration [1, 3]. To study the pool behavior more realistically, free pool surfaces have been incorporated and several numerical models have been proposed. Since the validity of the developed models should be judged based on practical measurements, pool surface sensing also plays an important role in numerical model development, which is recognized as the only way to acquire a thorough understanding of the physical processes occurring in the weld pool.

A possible application of pool surface shape sensing is the monitoring and control of weld quality, specifically of weld penetration. It is known that weld penetration control is a fundamental subject in automated welding. The difficulty associated with this problem is to find a precise and reliable way to measure the weld penetration using only top-side sensors that are attached to and move with the torch. Among the methods proposed in existing literature, pool oscillation [4–6] and infrared sensing [7, 8] based methods received more attention. (Ultrasonic sensing [9] and radiographic sensing [1] use additional sensing devices which are difficult to attach to the torch.) Acoustic emission sensing [10] can distinguish between full penetration and partial penetration. Though many methods are available to measure the weld penetration, in order to improve the quality of welding, new or improved solutions are still strongly needed due to the inherent restrictions associated with each of the above-mentioned methods. It has been noticed that a skilled human welder can extract penetration information by viewing the weld pool [11]. Due to the difficulty involved in on-line pool surface deformation sensing, the geometry of the weld behind the pool was measured as an alternative [12]. It was found that the average weld depression depth h, which is defined as the cross weld depression area divided by the weld width, has a close relationship with the full penetration state which is specified by the back-side bead width [11]. A corresponding closed-loop control system has been developed, and satisfactory control has been obtained [12]. However, there is an inherent measurement delay if the weld behind the pool is monitored rather than the pool itself [12]. If the pool surface deformation can be monitored, a promising weld penetration control strategy can be expected.

Although the pool surface shape sensing is important, a literature survey shows that limited work has been done in this area due to the extreme difficulty associated with this problem. The pioneering work was conducted at the Ohio State University by Rokhlin and Guu [1], using radiography. The radiation of the received x-ray increases with the depression depth. Using this approach, many valuable results have been acquired. However, only the case of stationary arc was addressed. To avoid the interference of electrode and gas nozzle, long electrode extension and inclined torch attitude were used. The imaging device and x-ray source could not both be attached to the torch to form a so-called top-side sensor. This fact, in addition to the radioactivity, restricts the prospective application of this method in practical monitoring or control of weld pools. Also, the principle behind this method is to measure the material thickness. For the case of full penetration where the back-side pool surface deformation occurs, the pool surface shape will be difficult to extract.

A novel mechanism for observing the pool surface shape was proposed by the present authors [13]. Laser stripes projected through a novel grid are reflected from and deformed by the mirror-like pool surface. The shape features of the weld pool surface are clearly shown by the reflection pattern. To apply this technology, the on-line acquisition of the reflection patterns and pool boundary is essential. In this work, the sensed image is analyzed and image processing is conducted. By the developed image processing technology, the reflection pattern and weld pool boundary can be acquired in real-time.

This paper is organized as followings. In section 2, a brief introduction is given to the sensing principle. Section 3 is dedi-

Contributed by the Manufacturing Engineering Division for publication in the JOURNAL OF MANUFACTURING SCIENCE AND ENGINEERING. Manuscript received April 1995; revised Sept. 1995. Associate Technical Editor: E. Kannatey-Asibu.

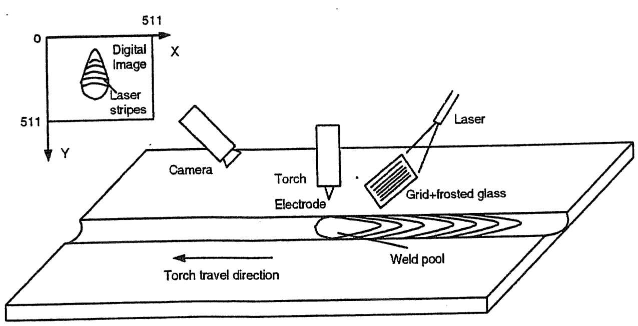

Fig. 1 Sensing mechanism of weld pool surface shape

cated to the acquisition of the weld pool boundary. In sections 4 and 5, laser stripes in the so called nonimpact and impact zones of the weld pool are detected respectively. The image processing results are illustrated using the acquired pool boundary and laser stripes in section 6. Finally, conclusions are drawn.

2 Principle and Sensor [13]

The proposed sensing system is shown in Fig. 1. A short duration pulsed laser is projected onto the weld pool. The camera shutter is synchronized with the pulse duration. During the laser pulse, the laser intensity is much stronger than the arc intensity, and the arc influence in weld pool observation is essentially eliminated [14]. To acquire the weld pool surface information, a special technique has been proposed to capture the specular reflection of the laser which passes through the grid onto the weld pool surface. The resultant images are shown in Fig. 2. It has been shown by the experiments that the reflected stripes are straight when a flat mirror is substituted for the weld pool. When a convex (concave) mirror is employed, the reflected stripes are convex (concave) as well. The pattern of the reflected stripes describes the reflection surface. Thus, the geometry of the reflected stripes contains the weld pool surface information.

3 Pool Boundary

Although a human can identify the boundary of the weld pool from the acquired image as shown in Fig. 2, its machine recognition may not be straightforward because of the complexity of the acquired image. In the acquired image, different scenes exist: torch, electrode, oxidized heat-affected zone (HAZ) edges, laser stripes, and boundary of the weld pool. To distinguish between these scenes, their inherent features, optical or geometrical or locational, must be found. Using the locational and optical features, torch and electrode have been successfully identified [15]. This accomplishment reduces the complexity in the further image analysis which distinguishes among laser stripes, HAZ edges, and weld pool boundary.

The boundary of the weld pool will be determined in two steps. In step 1, possible continuous edges are first detected in a region of interest which is selected based on the location of the torch and eletrode in the image. Then, the continuous edges corresponding to the boundary of the weld pool are distinguished from other continuous edges based on the inherent features of the different edge types (HAZ, stripe, etc.). Although the edges of the weld pool boundary can be identified, a complete boundary of the weld pool is still not acquired because of the overlap of the torch and electrode with the weld pool. Thus, in the second step, the acquired edges of the pool boundary will be used to fit a complete boundary for the weld pool.

3.1 Pool Edges. Divide the pool weld boundary into left and right edges. Denote the left and right edges as $x^{(l)} = x^{(l)}(y)$ $(y = y^{(l0)} + 0, \ldots, y^{(l0)} + K_l)$ and $x^{(r)} = x^{(r)}(y)$ $(y = y^{(r0)} + 0, \ldots, y^{(r0)} + K_r)$, respectively. The edges can be described by their point sets, i.e., $(x^{(l)}(y), y)$'s $(y = y^{(l0)} + 0, \ldots, y^{(l0)} + K_l)$ and $(x^{(r)}(y), y)$'s $(y = y^{(r0)} + 0, \ldots, y^{(r0)} + K_r)$. $(x^{(l)}(y^{(l0)}), y^{(l0)})$ and $(x^{(r)}(y^{(r0)}), y^{(r0)})$ are the initial points of the left edge and right edge. The numbers of the points contained in the left and right edges are $(1 + K_l)$ and $(1 + K_r)$, respectively. For a complete boundary of the weld pool, $K_r = K_l$. It can be seen that both $x^{(l)} = x^{(l)}(y)$ and $x^{(r)} = x^{(r)}(y)$ are single-valued functions. Thus, the left and right edges can be searched along the Y-axis direction using the following one-dimensional dynamic search algorithm.

Algorithm I: Assume $(x^{(0)}, y^{(0)})$ is given as the initial search point (Fig. 3). The Y-axis is the search direction. In the k^{th} $(k \geq 1)$ search, the initial search point is $(x^{(k-1)}, y^{(k-1)})$. The result $(x^{(k)}, y^{(k)})$ is defined by:

$$y^{(k)} = y^{(k-1)} + 1,$$

$$x^{(k)}\colon G(x^{(k)}, y^{(k)}) = \max_{x \in (x^{(k-1)} - \delta, x^{(k-1)} + \delta)} G(x, y^{(k)}) \tag{2}$$

where $G(x, y)$ is a gradient of the grayness along the X direction which could be specified as $G_{-x}(x, y)$ and $G_x(x, y)$, i.e., along the negative X axis and X axis directions according to the application. If $G(x^{(k)}, y^{(k)})$ is larger than the preset threshold T_g, the $(k + 1)^{\text{th}}$ search will be performed (Fig. 3). Otherwise, the dynamic search stops (Fig. 3), and the search length K is the current k. The resultant edge is $(x^{(k)}, y^{(0)} + k)$'s $(k = 0, 1, \ldots, K)$ (Fig. 3).

In the search for the left edge, the gradient has been defined as $G(x, y) = G_{-x}(x, y) = g(x - 1, y) - g(x + 1, y)$. For the

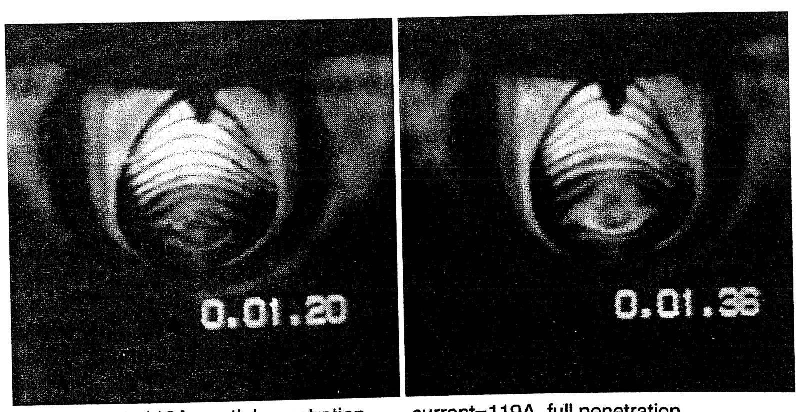

current=116A, partial penetration　　current=119A, full penetration

Fig. 2 Images acquired by the 3D vision sensor

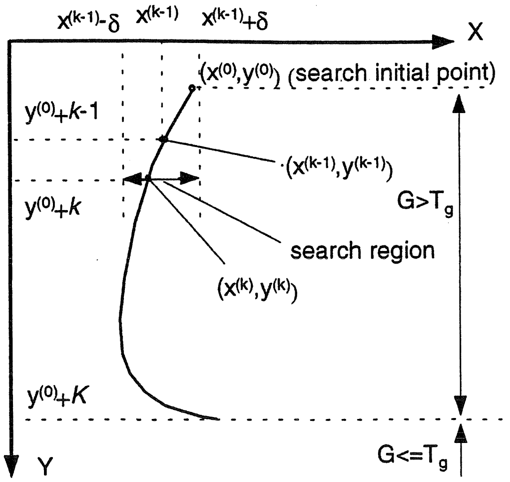

Fig. 3 One-dimensional dynamic search for pool boundary edge

right edge, $G(x, y) = G_x(x, y) = -(g(x-1, y) - g(x+1, y))$. Here $g(x, y)$ is the grayness of the point (x, y).

Consider the dynamic search for the right edge. It is observed that the contrast between the dark weld pool and bright solid region may vanish at the front of the weld pool because of the oxidation in the heat-affected zone (Fig. 2). The goal here is to detect the right edge until the contrast vanishes. If the initial point is correctly selected, this segment of the right edge will be detected by the proposed dynamic algorithm. However, the correct initial point is not easy to find. Thus, several initial points are chosen and used to find a number of continuous edges, and then the correct one is selected. Denote the eletrode-torch contours as $(i, etcontour[i])$'s $(i = M_1, \ldots, M_2)$ in the neighborhood of the electrode axis (Fig. 4). Because of the possible distance between the electrode-torch contours and the right edge of the weld pool (Fig. 4), potential initial points are selected as $(i, etcontour[i] + m)$'s $(i = b, \ldots, M_2)$, rather than $(i, etcontour[i])$'s $(i = b, \ldots, M_2)$. Here m is a positive integer and b (Fig. 4) was acquired when identifying the electrode-torch contours [15]. Among these possible initial points, only those points which have G_x greater than the threshold T_g are qualified. (If m is too small to overlap $(i, etcontour[i] + m)$'s on the weld pool, qualified initials may not be acquired. In this case, m should be increased until qualified initials are encountered.) The qualified initials can be classified into five types: pool edge point (Fig. 4), HAZ edge point (Fig. 4), convex stripe edge point (Fig. 4), concave stripe edge point, and surface defect zone edge point. For each of the qualified initial points, a dynamic edge search is performed using Algorithm I. Five types of edge could be acquired. It can be shown that the last two types of initials can only lead to short edges. Thus, if the length of the acquired edge is shorter than the threshold L_T, the edge is not taken as a candidate for the right edge. Assume that more than one long edge has been found. These edges are taken as the candidates. They are denoted as $(x_n^{(r)}(y), y)$'s $(1 \leq n \leq N, y_n^{(r0)} \leq y \leq y_n^{(K_r)})$ where N is the number of the candidate edges and the subscript n stands for the n^{th} candidate edge.

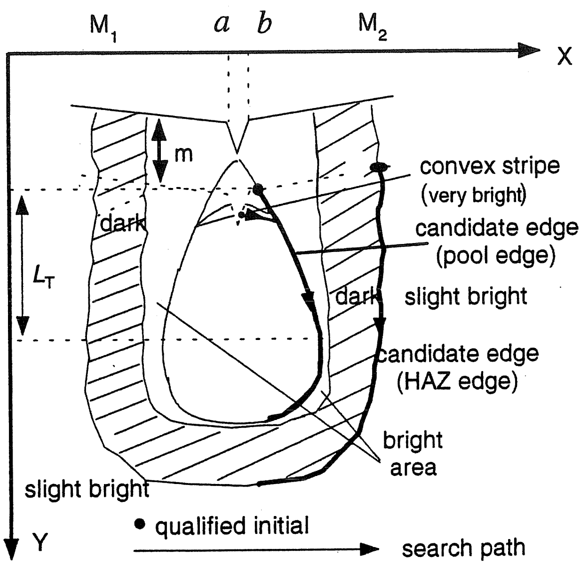

Fig. 4 Pool boundary right edge candidates

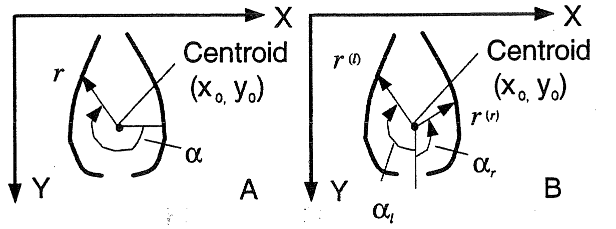

Fig. 5 Pool boundary description. A-Polar coordinate description. B-Piecewise polar coordinate description.

In order to identify the pool edge from other long candidate edges, the inherent features associated with different types of candidate edges must be investigated. For the convex stripe edge, its right neighborhood is the stripe. It is known that the stripe is much brighter than the grayness of the solidified area. Thus, the convex stripe edge can be distinguished from the right pool edge by examining the maximum grayness in the right neighborhood. For the remaining two types of long candidate edges, laser stripes can be expected at the left neighborhood of the right pool edge, whereas this is not true for a HAZ edge (Fig. 4). Because of the laser stripes, the largest grayness in its left neighborhood points $(x_n^{(r)}(y) - 10, y)$'s $(y_n^{(r0)} \leq y \leq y_n^{(K_r)})$ must be greater than the largest grayness in its right neighborhood points $(x_n^{(r)}(y) + 10, y)$'s $(y_n^{(r0)} \leq y \leq y_n^{(K_r)})$ for the right edge of the weld pool. Thus, if this is true, the corresponding long edge is accepted as the right edge $(x^{(r)}(y), y)$'s.

The selection of L_T is not critical since all the short edges, for example, the laser stripes' edges, are much shorter than the boundary edges.

By the proposed algorithms, the right edge of the weld pool can always be located with $m = 10$ and $L_T = 150$ in our experimentation. The algorithms can also be used to detect the left edge with a slight change in the gradient definition and the neighborhood direction. In the succeeding discussion, these edges of the weld pool will be used to determine the complete boundary of the weld pool.

3.2 Pool Boundary Fitting. To obtain the complete boundary from the acquired pool edges, a model should be used to describe the boundary. Different approaches may be used to describe closed boundaries [16]. For a closed boundary such as the pool boundary in which each radius vector from the centroid of the boundary intersects the boundary at only one point, a one-dimensional series of real numbers can be acquired by measuring the lengths of successive radius vectors which are angularly equispaced. This series is denoted as $\{r(\alpha)\}$'s where $r(\alpha)$ is the radius of the vector at the angle α (Fig. 5A). The boundary can be modeled by relating the radius to the angle. In this study, the following polar coordinate model is used to describe the pool boundary:

$$r(\alpha) = \theta_0 + \sum_{j=1}^{p} \theta_j \alpha^p = (1\ \alpha \ldots \alpha^p)\theta \tag{3}$$

where $\theta = (\theta_0, \theta_1, \ldots, \theta_p)^T$ is the parameter vector, and p is the order. It has been shown by modeling experimentation that it is very difficult to describe the pool boundary sufficiently even if a high p is used. However, the pool boundary can be described with sufficient accuracy using a low p if the boundary is modeled piecewisely. Define α_l and α_r as:

$$\left.\begin{aligned}\alpha_l &= \alpha - 90^\circ\\ \alpha_r &= -\alpha + 90^\circ\end{aligned}\right\}$$

The left and right boundary edges can be described by α_l and α_r separately (Fig. 5B). The corresponding models are:

$$r^{(l)}(\alpha_l) = \theta_0^{(l)} + \sum_{j=1}^{p} \theta_j^{(l)} \alpha_l^j = (1\ \alpha_l \ldots \alpha_l^p)\theta^{(l)} \tag{3l}$$

$$r^{(r)}(\alpha_r) = \theta_0^{(r)} + \sum_{j=1}^{p} \theta_j^{(r)} \alpha_l^j = (1\ \alpha_l \ldots \alpha_l^p)\theta^{(r)} \tag{3r}$$

The parameters are $\theta^{(l)} = (\theta_0^{(l)}, \theta_1^{(l)}, \ldots, \theta_p^{(l)})^T$ and $\theta^{(r)} = (\theta_0^{(r)}, \theta_1^{(r)}, \ldots, \theta_p^{(r)})^T$.

The measured data are provided by $(x^{(l)}(y), y)$'s $(y = y^{(l0)} + 0, \ldots, y^{(l0)} + K_l)$ and $(x^{(r)}(y), y)$'s $(y = y^{(r0)} + 0, \ldots, y^{(r0)} + K_r)$. Denote $\theta = \begin{bmatrix}\theta^{(l)}\\ \theta^{(r)}\end{bmatrix}$. The criterion for estimating the model parameters is:

$$\left.\begin{aligned}\theta^{(l)}:\ \min_{\theta^{(l)}\in R^{p+1}} \sum_{j=0}^{K_l} [d^{(l)}(j) - (1\alpha_l(j)\alpha_l^2(j)\alpha_l^3(j))\theta^{(l)}]^2 &= \min_{\theta^{(l)}} J^{(l)}(\theta^{(l)}\\ \theta^{(r)}:\ \min_{\theta^{(r)}\in R^{p+1}} \sum_{j=0}^{K_r} [d^{(r)}(j) - (1\alpha_r(j)\alpha_r^2(j)\alpha_r^3(j))\theta^{(r)}]^2 &= \min_{\theta^{(r)}} J^{(r)}(\theta^{(r)})\end{aligned}\right\} \tag{4}$$

where $d^{(l)}(j)$ and $d^{(r)}(j)$ are the distances from the origin (x_0, y_0) of the polar coordinate system to the left edge point $(x^{(l)}(y^{(l0)}+j), y^{(l0)}+j)$ and right edge point $(x^{(l)}(y^{(r0)}+j), y^{(r0)}+j)$ respectively. $\theta^{(l)}$ and $\theta^{(r)}$ can be calculated using the standard least squares algorithm [17].

To acquire the complete boundary from the left and right edge models, a smooth transition between the left and right edge region should be achieved. To do this, the data in the interval $(0 \le \alpha \le 180^\circ)$ can be used to fit a model for the front portion of the weld pool:

$$r^{(f)}(\alpha_f) = (1\ \alpha_f \ldots \alpha_f^p)\theta^{(f)} \tag{3f}$$

where $\alpha_f = \alpha$, and $\theta^{(f)} = (\theta_0^{(f)}, \theta_1^{(f)}, \ldots, \theta_p^{(f)})^T$. A weight-meaning method is proposed to construct the boundary of the weld pool from the acquired models (3l), (3r), and (3f) as shown by Fig. 6. For any α, the corresponding α_l, α_r, and α_f can be known. Using the models Eqs. (3l), (3r), and (3f), $r^{(l)}$, $r^{(r)}$, and $r^{(f)}$ can then be calculated for different angles α. Denote the corresponding values as $r^{(l)}(\alpha)$, $r^{(r)}(\alpha)$, and $r^{(f)}(\alpha)$. The intersection, $(\alpha_{\text{rear}}, r_{\text{rear}})$, of $r^{(l)}(\alpha)$ and $r^{(r)}(\alpha)$ is taken as the rear of the pool boundary (Fig. 6). Here $r_{\text{rear}} = r^{(l)}(\alpha_{\text{rear}}) = r^{(r)}(\alpha_{\text{rear}})$. The boundary of the weld pool $\{r(\alpha)\}$'s is calculated using the following equations:

$$\left.\begin{aligned}r(\alpha) &= r^{(l)}(\alpha) & (225^\circ < \alpha \le \alpha_{\text{rear}})\\ r(\alpha) &= r^{(r)}(\alpha) & (\alpha_{\text{rear}} < \alpha \le -45^\circ)\\ r(\alpha) &= w^{(r)}(\alpha)r^{(r)}(\alpha) + (1 - w^{(r)}(\alpha))r^{(f)}(\alpha) & (-45^\circ < \alpha \le 45^\circ)\\ r(\alpha) &= r^{(f)}(\alpha) & (45^\circ < \alpha \le 135^\circ\\ r(\alpha) &= w^{(l)}(\alpha)r^{(l)}(\alpha) + (1 - w^{(l)}(\alpha))r^{(b)}(\alpha) & (135^\circ < \alpha \le 225^\circ)\end{aligned}\right\} \tag{5}$$

where $w^{(l)}$ and $w^{(r)}$ are the weights:

$$\left.\begin{aligned}w^{(r)}(\alpha) &= 1 - (\alpha + 45^\circ)/90 & (-45^\circ \le \alpha \le 45^\circ)\\ w^{(l)}(\alpha) &= (\alpha - 135^\circ)/90 & (135^\circ \le \alpha \le 225^\circ)\end{aligned}\right\} \tag{6}$$

By using this weight-meaning method, reasonable boundaries of the weld pool can always be acquired with acceptable computation. The resultant boundary of the weld pool for the images in Fig. 2 are shown in Fig. 13 with other image processing results.

4 Stripes: Nonimpacted Zone

The deformation pattern of the reflected stripes provides critical information on the weld pool surface deformation. It can be observed in Fig. 2 that the reflection patterns are quite different in the nonimpacted zone and impacted zone. Thus, the weld pool is divided into nonimpacted and impacted zones (Fig. 7), respectively. The identification of the stripes will be performed at two zones respectively. In this section, the nonimpacted zone will be addressed.

Each stripe is enveloped by its upper and lower edges (Fig. 7). These upper and lower edges must be detected. If proper initials are used, these edges can be determined using the dynamic search algorithm proposed for the pool boundary edges with a slight modification. It is apparent that a different definition must be used for the gradient of the grayness corresponding to the upper and lower edge searches. Define gradient $G_y(x, y) = g(x, y+1) - g(x, y-1)$ for the upper edge and gradient $G_{-y}(x, y) = -(g(x, y+1) - g(x, y-1))$ for the lower edge search. A modified algorithm can be used for the edge search.

4.1 Search Algorithm.

Algorithm II: Assume $(x^{(0)}, y^{(0)})$ is given as the search initial point (Fig. 8A). The search direction could be either X-axis direction or negative X-axis direction. In the k^{th} $(k \ge 1)$ search, the search initial is $(x^{(k-1)}, y^{(k-1)})$. The resultant $(x^{(k)}, y^{(k)})$ for the upper edge is defined by:

$$\begin{aligned}x^{(k)} &= x^{(k-1)} + s,\\ y^{(k)}:\ G_y(x^{(k)}, y^{(k)}) &= \max_{y\in(\hat{y}^{(k)}-\delta, \hat{y}^{(k)}+\delta)} G_y(x^{(k)}, y)\end{aligned} \tag{7}$$

where $\hat{y}^{(k)}$ is the prediction to $y^{(k)}$, δ is a positive integer, and s is the search direction sign function. If the search direction is along the X-axis direction, the direction sign function $s = 1$. If the search is along the negative X-axis direction, the direction

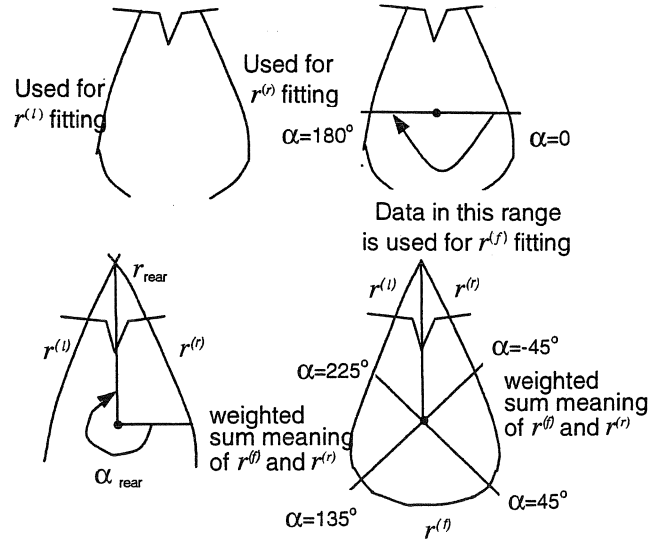

Fig. 6 Piecewise modeling of the weld pool boundary

sign function $s = -1$. If $G_y(x^{(k)}, y^{(k)})$ is larger than the threshold $T_g^{(u)}$ and the search does not exceed the region, the $(k+1)^{th}$ will be performed. Otherwise, the dynamic search stops, and the search length K is the current k. The resultant edge is $(x^{(0)} + ks, y^{(k)}$'s $(k = 0, 1, 2, \ldots, K)$ (Fig. 8*A*).

For the lower edges, the algorithm is similar.

4.2 Implementation. To implement Algorithm II, the search initials, search regions, thresholding, result evaluation, etc. must be addressed.

The search initials can be selected along the central line $x = x_0$. If $G_y(x_0, y) > T_g^{(u)}$ or $G_{-y}(x_0, y) > T_g^{(l)}$, point (x_0, y) can be selected as the initial point $(x^{(0)}, y^{(0)})$ for the upper edge or lower edge search, respectively. From these initial points, the search is performed along both the X and negative X axis directions. Thus, for one initial point, two segments of edge will be acquired (Fig. 8B). They are referred to as the left and right segments. These two segments are used to fit a 2^{nd} order polynomial by employing the standard least squares algorithm [17]. In the nonimpacted zone, both upper and lower edges are smooth and, as observed, can be well described by the fitted model. In the impacted zone, the extracted edge points can not be connected as a continuous segment. (This is shown in Fig. 12.) In this case, the extracted edge points cannot be accurately described by the fitted model. Thus, if significant modeling residual is encountered during fitting the upper or lower edge of a stripe, the stripe is considered the first stripe in the impacted

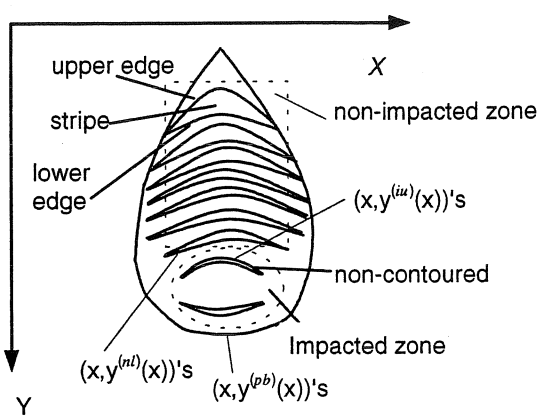

Fig. 7 Pool zones

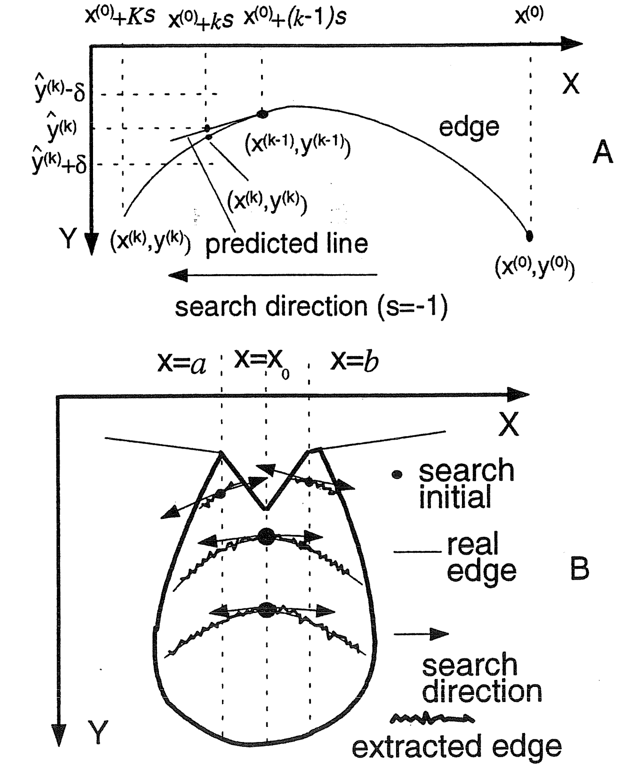

Fig. 8 Dynamic search for stripe edge. A-Iteration principle. B-Search initial and direction.

zone. The upper edge of this stripe is denoted by $(x, y^{(iu)}(x))$ where the superscript i and u stand for the impacted-zone and upper edge, respectively (Fig. 7). Its extraction will be discussed in the next section. The last stripe which passed the residual examination is taken as the last stripe of the nonimpacted zone. The lower edge of this last stripe, denoted by $(x, y^{(nl)}(x))$ (Fig. 7) where the superscript n stands for the nonimpacted zone and l for the last edge, will be used as the search template for $(x, y^{(iu)}(x))$.

It is observed that the torch-electrode shadow may block portions of some of the stripes. If this occurs, each affected stripe will be divided into two segments by the torch-electrode contour. For these edges, the search initials can not be acquired along the central line $x = x_0$. Thus, the initial points are selected at the lines $x = a$ and $x = b$ for the left and right segments of the stripes (Fig. 8*B*). For the left segment of the stripes, the search is performed along both the X-axis and negative X-axis directions (Fig. 8*B*). For the search along the negative X-axis direction, the search region is provided by the boundary of the weld pool (Fig. 8*B*). For the search along the X-axis direction, the search limit is the electrode-torch contour. Similarly, the search for the right segment of the stripes is also done along both directions and the search limits are provided by the boundary and electrode-torch contour (Fig. 8*B*). If interference occurs on more than one stripe, each left segment must be matched with its corresponding right segment. Thus, for each left segment, all the right segments are used to fit a model with the left segment, respectively. The one which generates the minimum residual is selected as the corresponding right segment for the considered left segment. Because only a few such stripes exist, maximum 2 as observed, the matching can be done with only slight computation. Thus, the stripes separated by the electrode and torch shadow can also be detected and modeled.

Because of the possible steep slope of the stripes, the prediction of the edge point to be searched is also important. Thus, the slope of the edge is recursively calculated with search marching.

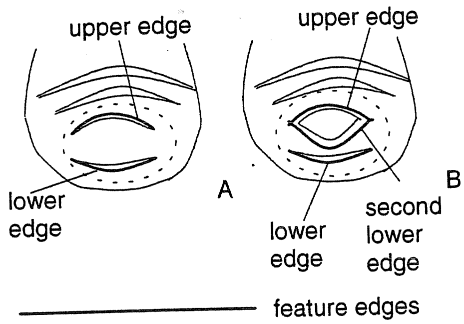

Fig. 9 Reflection modes and feature edges at the impacted zone. A-Open-contour mode. B-Closed-contour mode.

Denote $\rho^{(k-1)}$ for the slope calculated at the $(k-1)^{\text{th}}$ search. The prediction will be:

$$\hat{y}^{(k)} = y^{(k-1)} + s\rho^{(k-1)} \quad (8)$$

Once $y^{(k)}$ is acquired based on Eq. (7), the slope can be calculated using an autoregressive filter:

$$\rho^{(k)} = s(y^{(k)} - y^{(k-1)})(1-w) + w\rho^{(k-1)} \quad (9)$$

where w $(0 < w < 1)$. In the study, $w = 0.7$ has been selected. Thus, the edge point at the next search step can be predicted.

It can be seen that the grayness of the reflected stripes decays towards the front of the weld pool (Fig. 2). Also, it is known that the laser passes through the frosted glass [13]. A diffuse angle is therefore generated during the further travel of the laser. This diffuse angle plays a critical role in acquiring the reflection of the laser stripes in the image [13]. However, because of the diffuse angle, the intensity of the laser rays decays as the distance from the frosted glass to the reflection surface increases. Thus, the grayness of the reflected laser decreases towards the front of the weld pool. This varied grayness of the reflected stripes generates difficulty in selecting global threshold $T_g^{(u)}$ and $T_g^{(l)}$ for the dynamic searches. It is apparent that the values of the threshold should be reduced with increasing y. Adaptive thresholding is therefore proposed.

For any point (x, y) on the weld pool, one can find

$$M_y(x, y) = \max_{\substack{j \ge y \\ (x,j) \in S}} G_y(x, j),$$

$$M_{-y}(x, y) = \max_{\substack{j \ge y \\ (x,j) \in S}} G_{-y}(x, j) \quad (10)$$

where S is the set of the weld pool surface points. The thresholding can be determined based on $M_y(x, y)$ and $M_{-y}(x, y)$ for any point (x, y). The following thresholds have been successfully used to detect the edges of the reflected stripes:

$$T_g^{(u)}(x, y) = \max(0.6M_y(x, y), T_{\min}),$$

$$T_g^{(l)}(x, y) = \max(0.6M_{-y}(x, y), T_{\min}) \quad (11)$$

where $T_{\min}$ is the minimum gradient threshold.

Using the approach proposed, the reflection pattern in the non-impacted zone has been successfully detected. The detected edges for the images in Fig. 2 are illustrated in Fig. 13. No lower edges are illustrated in the figure due to the small distance and shape similarities between the lower edges and their adjacent upper edges.

5 Stripes: Impacted Zone

Plasma jets can generate a significant impact on the weld pool. The weld pool is therefore depressed. Roughly speaking, the center of the depressed area has the lowest point on the weld pool surface. From this center, the height of the weld pool surface increases along any direction. Thus, the slope of the weld pool surface changes sign in the depressed area. If the depression is significant, a laser stripe projected onto the depressed area could develop into a closed contour stripe. Thus, two modes of the reflected laser from the depression area are encountered, i.e., open-contour or closed-contour (Fig. 9).

An interesting phenomenon which can be observed from the impacted zone is the complexity of the reflection. Because of possible surface impurities, electrode tip irregularity, etc., the distribution of the impact of the plasma jet on the weld pool may not be perfectly smooth. Also, the high frequency components of the pool oscillation may influence the distribution of the plasma jet field. The nonuniform plasma jet distribution field and oscillated pool surface can be coupled. No stationary and smooth plasma jet distribution can be expected. As a result, the depressed surface may not be perfectly smooth. The local surface slope can severely change within a small region. Thus, the reflection may no longer exhibit the pure stripe mode as it does in the non-impacted zone (Fig. 2). In this case, the outline of the reflection as shown in Fig. 9 may be the only concern. This outline consists of the feature edges, i.e., two edges for the open-contour mode or three edges for the closed-contour mode. For the discussion convenience, the feature edges will be referred to as the upper edge, lower edge, and second lower edge, respectively (Fig. 9). The lower edge and second lower edge, if exists, will be referred to as the lower edges.

The proposed algorithm detects the edges in three steps. In the first step, the possible stripe edge points are detected and the reflection mode is examined. Then the stripe edge points are segmented into a number of continuous lines. In the third step, the segments are used to construct the edges.

5.1 Edge Detection. The search range for the edges is defined by $(x(1), x(2), \ldots, x(L))$ where $x(k) = x(1) - 1 + k$ $(k = 1, \ldots, L)$. To find this range, the maximum grayness $g_m(x)$ between the $(x, y^{(nl)}(x))$ and $(x, y^{(pb)}(x))$ is searched:

$$g_m(x) = \max_{y^{(nl)}(x) \le y \le y^{(pb)}(x)} g(x, y) \quad (12)$$

where $(x, y^{(pb)}(x))$ is the front edge point of the weld pool boundary (Fig. 7). The acquired curve is illustrated in Fig. 10. Because of the significant difference in the grayness between the dark area and reflection area, a grayness threshold can be easily found to distinguish the reflection point from the non-reflection dark point. Thus, the range can be determined (Fig. 10).

Define

$$T_g^{(u)}(x) = 0.6M_y(x, y^{(nl)}(x)) \quad (13)$$

and

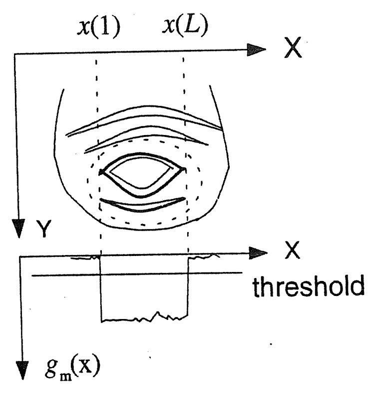

Fig. 10 Search range determination for edges at impacted zone

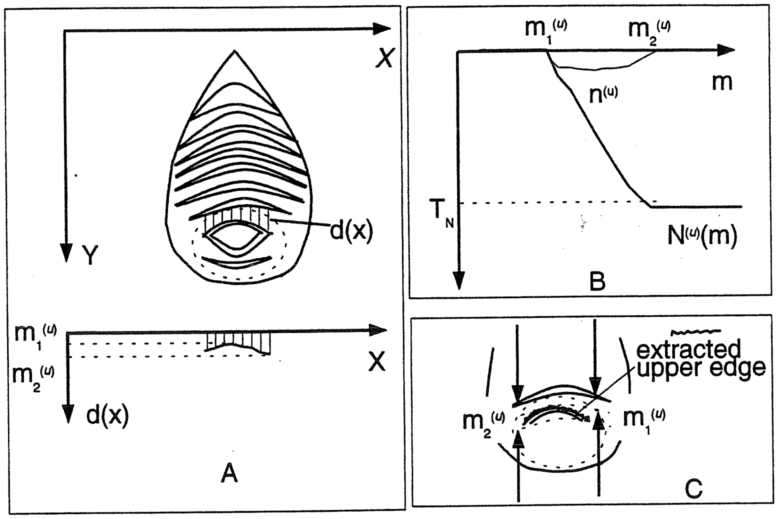

Fig. 11 Illustration of the upper edge detection at impacted zone. A-edge shape similarity. B-Region determination. C-Resultant edge points.

$$n^{(u)}(m) = \sum_{x=x(1)}^{x(L)} f(x, y^{(nl)}(x) + m) \tag{14}$$

where

$$\left. \begin{array}{l} f(x, y) = 1 \text{ when } g(x, y) > T_g^{(u)}(x) \\ f(x, y) = 0 \text{ when } g(x, y) \le T_g^{(u)}(x) \end{array} \right\}$$

It is known that the upper edge to be detected is convex despite the stripe mode. Because of this similarity in the shape, the change in the distance between $(x, y^{(iu)}(x))$ and $(x, y^{(nl)}(x))$, i.e., $d(x) = |y^{(iu)}(x) - y^{(nl)}(x)|$, is slight. Denote this region as $(m_1^{(u)} \le d(x) \le m_2^{(u)})$ (Fig. 11A). Define

$$N^{(u)}(m) = \sum_{k=1}^{m} n^{(u)}(k)$$

Thus, $N^{(u)}(m_2^{(u)})$ should reach L. To find the region, $m_2^{(u)}$ can be first determined using the following criterion:

$$m_2^{(u)} = \min_{M \in I^+} M : N^{(u)}(M) \ge T_N \tag{15}$$

where I^+ is the set of positive integers, and T_N is a positive integer threshold. Ideally, one should select $T_N = L$. However, small unmolten impurity particles may exist on the weld pool surface. The reflection may be influenced slightly. To raise the robustness of the algorithm, $T_N = 0.9L$ has been selected. Fig. 11B shows the principle of the above operation. Once $m_2^{(u)}$ is acquired, $m_1^{(u)}$ can then be determined employing the equation below:

$$m_1^{(u)} = \min_{1 \le m \le m_2^{(u)}} m : n^{(u)}(m) \ge 1 \tag{16}$$

The resultant $m_1^{(u)}$ is also illustrated in Fig. 11B. In Fig. 11C, the extracted upper edge points are illustrated.

If the second lower edge appears, the lower edge may lie in its neighborhood (Fig. 2). The image analysis tends to be complicated. To analyze the image, the stripe mode, i.e., open-contour or closed-contour, should be de determined.

Denote

$$T_g^{(l)}(x) = 0.6 M_{-y}(x, y^{(nl)}(x)) \tag{17}$$

Define the function

$$n^{(l)}(m) = \sum_{x=x(1)}^{x(L)} f(x, y^{(pb)}(x) - m) \tag{18}$$

where

$$\left. \begin{array}{l} f(x, y) = 1 \text{ when } g(x, y) > T_g^{(l)}(x) \\ f(x, y) = 0 \text{ when } g(x, y) \le T_g^{(l)}(x) \end{array} \right\}$$

Select $m_2^{(l)}$ by the following equation:

$$\min_{x(1) \le x \le x(L)} [y^{(pb)}(x) - m_2^{(l)}] = \max_{x(1) \le x \le x(L)} [y^{(nl)}(x) + m_2^{(u)}] \tag{19}$$

If the closed-contour has been developed, the second lower edge will be close to the lower edge. The sum $N^{(l)}(m_2^{(l)}) = \sum_{m=1}^{m_2^{(l)}} n^{(l)}(m)$ will be close to $2L$, rather than L. Because of the significant difference in the sum, $N^{(l)}$ can be used to classify the reflection mode reliably, despite possible image noise and imperfection. If $N^{(l)}(m_2^{(l)}) \le 1.5L$, the mode is open-contour. Otherwise, the closed-contour exists.

5.2 Segmenting. Denote the resultant upper edge points by $(upperx[i], uppery[i])$'s $(i = 1, \ldots, I^{(u)})$. Here the log i increases with the y if more than one upper edge point exists at the same x coordinate. Also, i increases with x. Similarly, the points of the lower edges, which include the second lower edge in the case of closed-contour mode, are denoted by $(lowerx[i], lowery[i])$'s $(i = 1, \ldots, I^{(l)})$.

Select $(upperx[1], uppery[1])$ as the initial point for segmenting the upper edge points. Assume that the current edge point is $(upperx[k], uppery[k])$. Denote

$$d_i = |uppery[k] - uppery[i]| + upperx[i] - upperx[k] \quad (i = k+1, \ldots,)$$

If

$$d_{i*} = \min d_i < d_{\max} \; (i = k+1, \ldots,),$$

$(upperx[i*], uppery[i*])$ and $(upperx[k], uppery[k])$ are considered to be the same segment. (Here the positive integer $d_{\max}$ is the continuity threshold, i.e., the maximum allowed distance between two adjacent points of a continuous segment.) In this case, let $k = i*$. The search for the remaining portion of the current segment continues. Otherwise, $(upperx[k], uppery[k])$

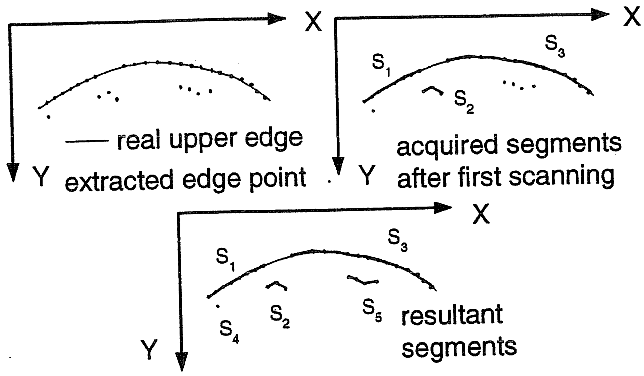

Fig. 12 Segmenting of upper edge points

is recognized as the ending point of the current segment and a new segment is searched. Before $(upperx[I^{(u)}], uppery[I^{(u)}])$ is reached, $(upperx[k+1], uppery[k+1])$ is used as the initial point for the new segment. If $(upperx[I^{(u)}], uppery[I^{(u)}])$ is reached, all the upper edge points must have been scanned once. This is referred to as the first scanning (Fig. 12). In the first scanning, some points in $(upperx[i], uppery[i])$'s may not be contained in any of the segments (Fig. 12). If such points exist, the second scanning will be performed. The initial point will be the one with the least log i in such points. The points which have been contained in the extracted segments in the first scanning are also used in the second scanning. (However, these points can not be used as the initial points.) Thus, the scanning can be performed until all the upper edge points are contained in at least one segment (Fig. 12).

For the points of the lower edges, the segmenting can be completed similarly despite the stripe modes.

5.3 Recognition. Assume that $S_k^{(u)}$'s $(k = 1, \ldots, K^{(u)})$ and $S_k^{(l)}$'s $(k = 1, \ldots, K^{(l)})$ are the resultant candidate segments for the upper edge and lower edges, respectively. To determine the final reflection pattern at the depressed area, the shape credits of the candidate segments are first calculated. The shape credit $c_s(k)$ of candidate segment k can be calculated using the second-order derivatives. It is known that the upper edge should have a positive second-order derivative, whereas the lower edges should have negative second-order derivatives in the image coordinate system. If the second-order derivative is larger than 0 at a point of the considered segment, the shape credit will be increased by 1. For 0 or negative second-order derivative, the shape credit will be increased by 0 and -1, respectively.

Consider the upper edge. If the shape credit is negative, the segment is deleted from the candidate segments. In the remaining segments, the longest segment is first used to fit the following model:

$$y = \sum_{j=0}^{p} \beta(j) x^j \tag{20}$$

where $\beta = (1, \beta_1, \ldots, \beta_p)^T$ is the model parameter vector, and p is the order. The parameters can be identified using the standard least squares algorithm [17]. Once the parameters are identified using the points of the longest segment, the succeeding longest segment is added to fit a new model. In order to do this, an algorithm must be developed to calculate the new parameters with a slight increase in the computation for the purpose of the on-line implementation. Also, a criterion is needed to determine the acceptance or rejection of the added segments. Thus, an identification approach has been proposed to select the added segment and acquire the new parameters. By using the proposed identification approach, the upper edge segments have been successfully selected.

It is apparent that the lower edge can also be acquired similarly if the open-contour mode is encountered. In the case of the closed-contour mode, the longest segment is selected first. Then the second longest segment is compared with the longest segment in terms of the horizontal region. If overlapping exists between these two regions, the first and second longest segments must be on different edges. They can be taken as the initial segments for the two lower edges, respectively. Otherwise, the horizontal regions of the longest and succeeding longest segments are examined until the overlapping is encountered. Thus, the initial segments for the two lower edges can be acquired. If the new segment can reduce the modeling error for any edge, the segment is accepted to the corresponding edge. Otherwise, the segment is deleted.

By using the proposed identification approach, all the edges have been successfully determined (Fig. 13). Hence, the reflection pattern at the depressed area is acquired.

6 Results of Image Processing

In general, the results of the image processing are quite satisfactory (Fig. 13). The parameters of the fitted models for the stripe edges and pool boundary provide a description of the free pool surface. Using these parameters, the free weld pool surface can be reconstructed based on the reflection law [18, 19]. Also, because of the unique relationship between the weld pool surface and reflection pattern, the reflection pattern can be directly used to control the weld penetration without surface shape calculation. This work is currently under investigation.

Extensive experimentation has shown that the image processing can always be completed in 210 ms with a 486DX 100. The time required for the electrode-torch and pool boundary

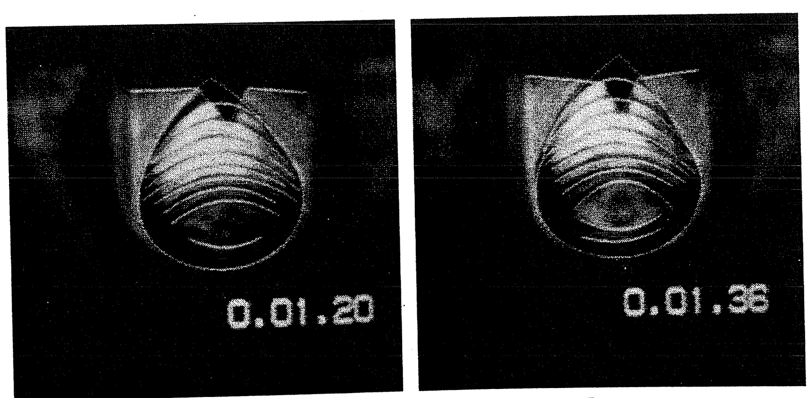

A B

Fig. 13 Processed images. A-Open-contour image. B-Closed-contour image.

extraction and modeling is approximately equal to the time needed for the extraction and modeling of the laser stripe edges in the weld pool. It is known that the frame grabbing for standard video signal is 33.3 ms. Thus, the free weld pool can be monitored at 4 Hz. This speed has been sufficient for the weld penetration control in gas tungsten arc welding [12, 14]. It has been shown that the proposed approach for segment selection and edge modeling made it possible to acquire robust estimates of the impacted zone edges with acceptable computation. Despite the achieved speed, an advanced processor is being used to promote the speed to 10 Hz in order extend the developed free pool surface monitoring technology to more applications.

7 Conclusions

The monitoring of the free weld pool surface is an important issue for studying and controlling the welding processes. However, due to the strong arc and the mirror-like surface, limited achievement has been made. The novel sensing system proposed by the authors provides a solution. By the image processing technology developed in this work, the weld pool surface deformation can be monitored in real-time. Currently, this technology is used to correlate the weld penetration to the reflection pattern, especially the reflection pattern at the impacted zone.

Acknowledgment

This work is supported by the National Science Foundation under contract DMI-9414530.

References

1 Rokhlin, S. I., and Guu, A. C., 1993, "A Study of Arc Force, Pool Depression, and Weld Penetration during Gas Tungsten Arc Welding," *Welding Journal,* Vol. 72, No. 8, pp. 381s–390s.

2 Lin, M. L., and Eagar, T. W., 1983, "Influence of Surface Depression and Convection on Arc Weld Pool Geometry," *Transport Phenomena in Material Processing,* ASME PED 10, Edited by M. M. Chen, J. Mazumder, and C. L. Tucker III, November 13–18, pp. 63–69.

3 Lin, M. L., and Eagar, T. W., 1985, "Influence of Arc Pressure on Weld Pool Geometry." *Welding Journal,* Vol. 64, No. 6, pp. 163s–169s.

4 Renwick, R. J., and Richardson, R. W., 1983, "Experimental Investigation of GTA Weld Pool Oscillations," *Welding Journal,* Vol. 62, No. 2, pp. 29s–35s.

5 Zacksenhouse, M., and Hardt, D. E., 1983, "Weld Pool Impedance Identification for Size Measurement and Control," ASME *Journal of Dynamic Systems, Measurement and Control,* Vol. 105, No. 3, pp. 179–184.

6 Xiao, Y. H., and Ouden, G. den, 1993, "Weld Pool Oscillation During GTA Welding of Mild Steel," *Welding Journal,* Vol. 72, No. 8, pp. 428s–434s.

7 Nagarajan, S., Banerjee, P., Chen, W., and Chin, B. A., 1992, "Control of the Welding Process Using Infrared Sensors." *IEEE Transactions on Robotics and Automation,* Vol. 8, No. 1, pp. 86–93.

8 Beardsley, H. E., Zhang, Y. M., and Kovacevic, R., 1994, "Infrared Sensing of Full Penetration State in Gas Tungsten Arc Welding," *International Journal of Machine Tool and Manufacturing,* Vol. 34, No. 8, pp. 1079–1090.

9 Carlson, N. M., and Johnson, J. A., 1988, "Ultrasonic Sensing of Weld Pool Penetration," *Welding Journal,* Vol. 67, No. 11, pp. 239s–246s.

10 Cannon, I., Maram, J., and Smith, M., 1987, "Weld Penetration Sensor for an Experimental Welder." *Transactions of NAMRC/SME,* Vol. XV.

11 Zhang, Y. M., et al., 1993, "Determining Joint Penetration in GTAW With Vision Sensing of Weld Face Geometry." *Welding Journal,* Vol. 72, No. 10, pp. 463s–469s.

12 Zhang, Y. M., Kovacevic, R., and Wu, L., 1996, "Dynamic Analysis and Identification of Gas Tungsten Arc Welding for Weld Penetration Control," ASME Journal of Engineering for Industry, Vol. 118, No. 1, pp. 123–136.

13 Kovacevic, R., Zhang, Y. M., and Ruan, S., 1993, "Three-Dimensional Measurement of Weld Pool Surface," *Proceedings of the International Conference on Modeling and Control of Joining Processes,* pp. 600–607, Orlando, FL, Dec. 8–10.

14 Kovacevic, R., Zhang, Y. M., and Ruan, S., 1995, "Sensing and Control of Weld Pool Geometry for Automated GTA Welding," ASME Journal of Engineering for Industry, Vol. 117, No. 2, pp. 210–222.

15 Zhang, Y. M., Beardsley, H., and Kovacevic, R., 1994, "Real-Time Image Processing for 3D Measurement of Weld Pool Surface," *Manufacturing Science and Engineering,* PED-Vol. 68-1, pp. 255–262, ASME.

16 Kashyap, R. L., and Chellappa, R., 1985, "Stochastic Models for Closed Boundary Analysis: Representation and Reconstruction," *Digital Image Processing and Analysis,* Vol. 2, pp. 109–119, R. Chellappa, and A. A. Sawchuk, eds., *IEEE Computer Society.*

17 Pandit, S. M., and Wu, S. M., 1983, "Time Series and System Analysis with Applications," Chapter 2, John Wiley and Sons, New York.

18 Kovacevic, R., and Zhang, Y. M., "Sensing Free Surface of Arc Weld Pool Using Specular Reflection: Principle and Analysis," to appear in *Proc Instn Mech Engrs,* Part B, *Journal of Engineering Manufacture.*

19 Kovacevic, R., and Zhang, Y. M., 1996, "Apparatus and Method for Measuring 3-D Weld Pool Shape," United States Patent, #5,481,085, January. 2.